NMR velocity mapping of gas flow around solid objects

Song-I Han,* Kimberly L. Pierce, and Alexander Pines
Materials Science Division, Lawrence Berkeley National Laboratory and Department of Chemistry, University of California, Berkeley, California 94720, USA

(Received 23 October 2005; published 13 July 2006)

We present experimental visualizations of gas flow around solid blunt bodies by NMR imaging. NMR velocimetry is a model-free and tracer-free experimental means for quantitative and multi-dimensional flow visualization. Hyperpolarization of ^{129}Xe provided sufficient NMR signal to overcome the low density of the dilute gas phase, and its long coherence time allows for true velocity vector mapping. In this study, the diverging gas flow around and wake patterns immediately behind a sphere could be vectorally visualized and quantified. In a similar experiment, the flow over an aerodynamic model airplane body revealed a less disrupted flow pattern.

DOI: 10.1103/PhysRevE.74.016302 PACS number(s): 47.60.+i, 76.60.Pc, 47.80.−v

INTRODUCTION AND BACKGROUND

The study of aerodynamics is crucial for many topics related to our modern lives from airplanes and sports to the understanding of chemical processes. Despite great efforts towards simulating complicated fluid dynamics, the need for experiments is crucial. Among the approaches, the magnetic resonance imaging (MRI) flow imaging modality is the most versatile, direct, and quantitative method, the basis for its establishment in the medical field. However, it has just recently begun to be recognized as a unique means for studying flow processes and catalysis in chemical engineering applications [1,2]. Wide application of NMR velocimetry in fluid dynamics studies has been hampered by the high cost of NMR equipment and, until recently, the lack of sophisticated visualization techniques. Improvements along both of these fronts are developing NMR velocimetry's potential to become an important tool to study fluid dynamics problems [2].

Not surprisingly, there remains a relatively poor understanding of the strength and limitations of NMR velocimetry among nonspecialists. One common source of confusion arises from the disparity between experimental duration and velocity encoding. Typically, NMR imaging methods are performed in two- or three-dimensional fashion, making the total experimental time as long as tens of minutes or more. The lengthy experimental time is due especially to the repetition time, typically ~0.5–1 s, required for recovery of equilibrium between each scan for multi-dimensional encoding or signal accumulation. However, a velocity profile along only one spatial dimension, analogous to those which are commonly obtained by non-NMR velocimetry techniques, can be obtained as fast as 0.02–2 s, making it comparable to the limitations of state-of-the art velocity mapping tools based on ultrasound techniques [3,4]. Velocities in a range of 100 μm/s and 10 m/s can be captured within a 100 μs "exposure time" (gradient pulse duration), with limitations and time costs that are comparable to or better than modern non-NMR techniques capable of spatially mapping velocities. However, NMR velocimetry techniques cannot provide an ultra-fast snapshot of the whole flow setup like some optical methods can, so that only flow dynamics that are time invariant within the total experimental time can be accessed. While optical methods can operate at high speed, the capability does not come without a price, namely they are mostly not applicable for opaque fluids and/or flow vessels, the information can be strictly qualitative (high-speed camera), instantaneous velocities are measured within a 10–50 μm^3 volume element with no fine spatial resolution [laser doppler velocimetry (LDV)], and the detection system needs to be designed and optimized for each flow setup, which is extremely difficult for complex geometries [LDV, particle image velocimetry (PIV)]. Additionally, most nonmagnetic resonance methods are invasive, requiring the use of tracer particles, dye molecules, or inserted probes. Modern variations of ultrasound-based velocimetry techniques are capable of mapping the flow field directly without prior knowlede of the flow field and are applicable to opaque media, e.g., [3,4], but face technical difficulties in convoluted geometries. One important aspect of NMR velocimetry technique is that it is a true three-dimensional technique in that either full three-dimensional flow maps or two-dimensional flow maps within a selected slice as thin as 200 μm can be obtained without extra effort or hardware modification. However, it should be noted that the first is time-consuming (~3 h or more), and the latter requires high signal sensitivity, which is given if the medium is, e.g., the ^{1}H of water or highly hyperpolarized ^{129}Xe noble gas. Another unique feature of MRI velocimetry is its ability to provide quantitative velocity maps, without the use of tracer particles or physical models, a characteristic which makes it a noninvasive and direct technique [6–10]. This is because the NMR signal originates from the nucleus of choice, as part of the material of interest, based on its magnetic resonance properties, namely its Larmor frequency, ω_0, polarization, and coherence lifetime. The radio frequency circuitry at a given static magnetic field, $\mathbf{B}_0$, can be adjusted such that only the chosen nucleus, as part of the fluid phase, is visible to the detector, making it blind to the device material and geometry. Because the NMR signal not only possess polarization (signal amplitude) but also coherence (phase coherence in an ensemble of spins) with a considerable life

*Current address: University of California Santa Barbara, Department of Chemistry and Biochemistry, Santa Barbara, CA, 93111.

time, the nuclei can be encoded with information that can be read out after a so-called encoding time that can vary anywhere between 500 μs and 1 s. This allows the direct determination of the velocities without the use of models within the mentioned range of 100 μm/s to 10 m/s and higher, where the upper limit is given by the length of the NMR detector divided by a short encoding time and the lower limit by thermal diffusion of the fluid. Furthermore, the unique magnetic signature of a nucleus makes it possible to distinguish the chemical composition of the fluid phase. This, together with the multidimensional nature of NMR, allows flow imaging of multiphase and multicomponent systems in a chemically selective manner [11,12].

The principle of spatial encoding is based on the use of magnetic field gradients, $\mathbf{G}(\mathbf{r})=\nabla\mathbf{B}$, so that spins at a given location, $\mathbf{r}$, acquire a unique NMR frequency, ω_0, as given by the Larmor relationship: $\omega_0(\mathbf{r})=\gamma|\mathbf{B}_0|+\gamma\mathbf{G}(\mathbf{r})\cdot\mathbf{r}$, where γ is the gyromagnetic ratio of the nucleus. Further, $\mathbf{G}(\mathbf{r})$ can be manipulated in such a way that velocity encoding can be realized. The complex nature of the NMR signal is exploited to make the phase linearly dependent on translational velocity by delivering, in the simplest case, two gradient pulses of same pulse duration, δ, and opposite amplitude, G, with a time separation, Δ. For static spins, the second gradient pulse refocuses the effect of the first gradient pulse; however, any spin which is moving during the time separation, Δ, will gain a net phase, ϕ corresponding to its velocity, v, given by, $\phi=\gamma\cdot\delta\cdot G\cdot\Delta\cdot v$. This phase dependency can deliver the complete velocity distribution by mapping out the Fourier space with a series of NMR signal amplitudes. However, a much less time-consuming method is to directly calculate the phase value so that a 2D spatial representation of velocities is obtained by a single 2D experiment. The phase shift, ϕ, in each pixel of the image ideally depends only on the local spin translational velocity component of choice. However, imperfect performance of the MRI hardware may lead to additional phase artifacts, ϕ'. Assuming these errors are the same throughout the experiment, the corrected velocity value can be obtained,

$$\frac{S_1}{S_2}=\frac{|a_1|\exp(i\phi_1)\exp(i\phi')}{|a_2|\exp(i\phi_2)\exp(i\phi')}=\frac{|a_1|}{|a_2|}\exp[i\cdot(\phi_1-\phi_2)]$$

where S_1 and S_2 are two complex NMR signals obtained with different velocity encoding gradient values, G, and a_1 and a_2 are the corresponding signal amplitudes. In summary, the combination of this fast velocity mapping technique with hyperpolarization of ^{129}Xe gas in continuous flow mode allowed us to obtain 4D velocity vector maps, composed of two spatial and two velocity dimensions.

There are several examples in the literature where similar 4D vector maps have been used to visualize fluid dynamics problems in the liquid phase [8,10]. However, gases remain a rare medium of investigation primarily due to the lack of sensitivity at low density. Most MRI gas studies utilize laser-polarized noble gases [11–18], thermally polarized fluorinated gases, such as SF_6 [10,19], or dense hydrocarbons [20,21]. While each of these media has its applications, ^{129}Xe has the advantage of being inert and capable of delivering information about its local chemical environment [11,12]. Additionally, ^{129}Xe has an unusually long coherence and polarization lifetime, which not only allows for a full velocity vector mapping, but also makes it a versatile information carrier to trace a selected fluid bolus for seconds. Such a tracer has proven useful in systems such as flow through porous media, where the spatial development of fluid dispersion is unpredictable, as recently shown in remote reconstruction of gas flow through porous media [22]. Yet there are limited reports of hyperpolarized ^{129}Xe gas being used for quantitative dynamics studies, and the acquisition of true velocity vector images of gas flow has not been previously reported. Such a measurement is only feasible with ^{129}Xe gas, which provides long coherence time and thus a long encoding time and phase stability to the NMR signal. The noble gas, ^{3}He, can also be highly polarized and possess an even higher signal amplitude and longer lifetime, which is why it is regarded as a valuable tool for lung void space visualization. However, ^{3}He cannot be employed for NMR velocimetry applications because it cannot be produced in a continuous flow mode, as the hyperpolarized ^{129}Xe gas in this work. Recent studies with SF_6 have delivered flow maps at impressively high Reynolds numbers (Re) [10] and lung tissue images [19], but its extremely short coherence lifetime limits the ability to use NMR parameter filters, select slices, and fully exploit the complex NMR phase for information encoding.

In the literature, experimental, computational, and theoretical studies of gas flow dynamics do not often come to a unified conclusion, mainly due to the lack of quantitative, model-free, and noninvasive experimental means on the one hand, and the lack of computational power on the other. One classic example in fluid dynamics is flow over a sphere in a duct. While the low Reynolds number flow regime is fully understood, there is little agreement on under what conditions flow patterns such as periodic vortex shedding and recirculation flow in this system [23–28] are observed, and over what Re regime transitions to asymmetry of flow and spatially invariant oscillatory patterns are observed. Experimental investigations of Re up to 5×10^6 [27] have been reported. The range of agreement is that periodic shedding should begin somewhere around Re=270 to 300 [25], but periodicity has been observed as low as Re=130 [28] and as high as Re=6000 [27]. Regardless of the shape of the far wake, the region immediately behind the sphere is characterized by a fairly symmetric region of low-amplitude longitudinal flow. At moderate Re this often contains recirculation components, unless $\mathrm{Re}\ll1$, where balanced forces result in the reversibility of flow making the leading and trailing streamlines identical [5].

EXPERIMENTAL DETAILS

As a model of the sphere in a duct, a 1 cm blown-glass ball was centered in a 30 cm long glass cell (2 cm i.d.), suspended by a 0.3 cm glass rod. Another cell had affixed to its wall the aerodynamic body of a model MDD DC-10 toy airplane. A region of interest centered at the ball, including

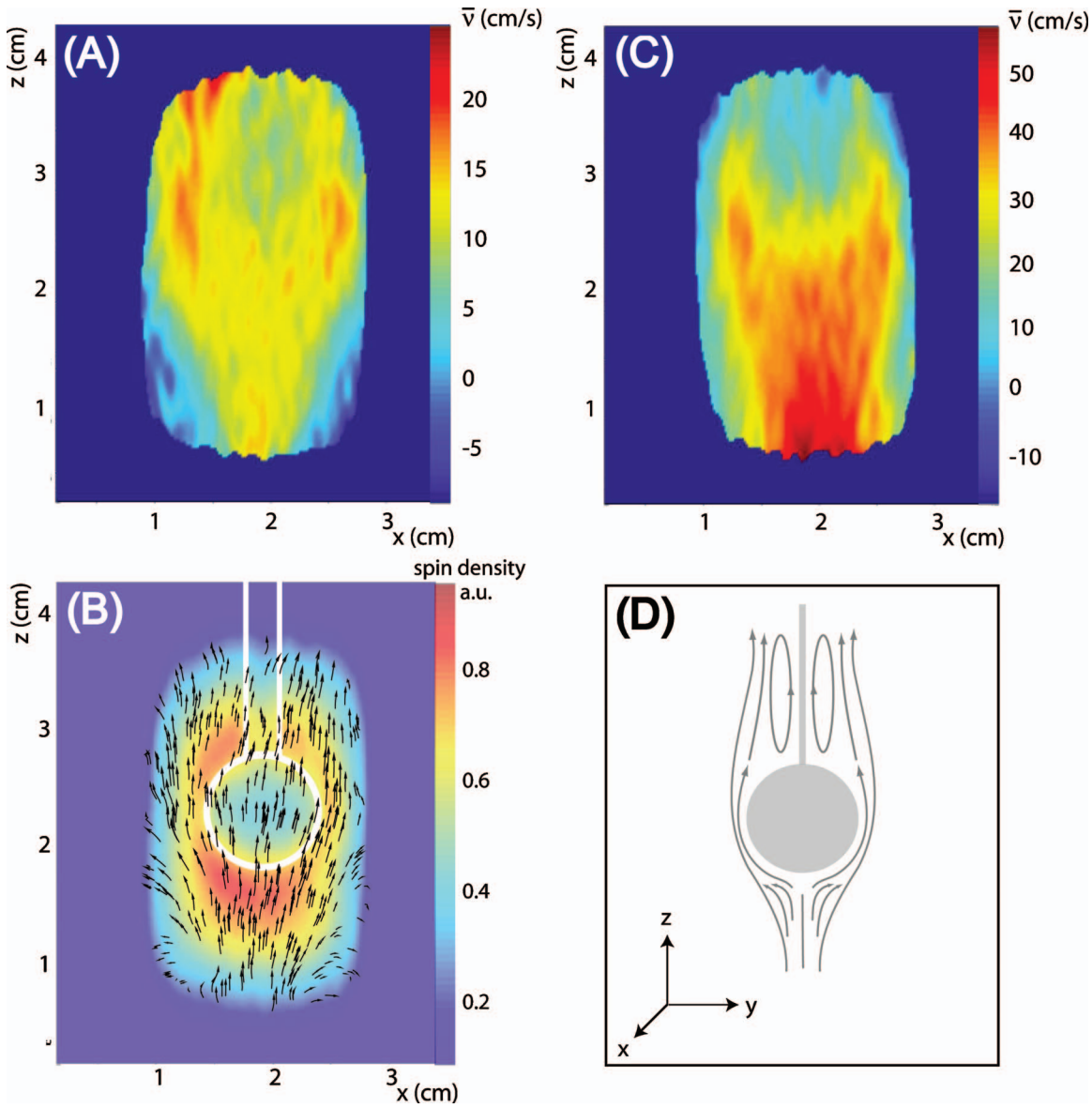

FIG. 1. (Color) ^{129}Xe MRI velocity maps (a–c) of flow around a sphere in a duct acquired with 128×64 points. The overall pattern reveals coherent characteristics that are slower than the echo time and remains after averaging over the experimental time. (a) Velocity map of v_z as a function of z and x spatial coordinates at Re=100 with a maximum velocity of around 18 cm/s (b) 4D vector plot of v_z and v_x (not shown) velocity components as a function of z and x spatial coordinates. Each vector represents an averaged result over several pixels. (c) Velocity map of v_z as a function of z and x coordinates at Re=200 with a maximum velocity around 40 cm/s. (d) A sketch of the diverging streamlines around the ball and recirculation eddies behind the ball as expected for Re$>$1 and the spatial coordinates used for all experiments.

the interaction of the gas front with the sphere and the wake immediately behind, was chosen with the intention of visualizing the most reported dynamics and framing a spatial reference with the centered sphere. A schematic of the cell and axis coordinate is presented in Fig. 1(d). The MRI experiments were performed in the 4.2 T field (^{129}Xe ω=49.8 MHz) of a Nalorac super wide bore ($\varnothing$=15 cm) magnet equipped with a Chemagnetics spectrometer and a Doty clear bore probe ($\varnothing_{coil}$=2.5 cm) with built-in x, y, and z magnetic field gradient coils. Here, z is the axis of the main static magnetic field and the primary gas flow direction.

Average velocities ranged from 10 to 20 cm/s, as calculated from the volume flow rate for the given geometry and measured by NMR velocimetry. The flowing gas was a mixture of natural abundance ^{129}Xe, N_2, and He gases in a 1:2:3 ratio, pressurized to 7 atm. ^{129}Xe was polarized by spin exchange optical pumping with Rb vapor [29] using a home-built continuous-flow polarizer as previously described [30]. Typical polarizations achieved for these experiments are 1–10%. Measurements at two different Re regimes are presented for the sphere in the duct: one around 100, which may be just around the transition to symmetric, periodic vortex shedding [25], and the other determined by NMR measure-

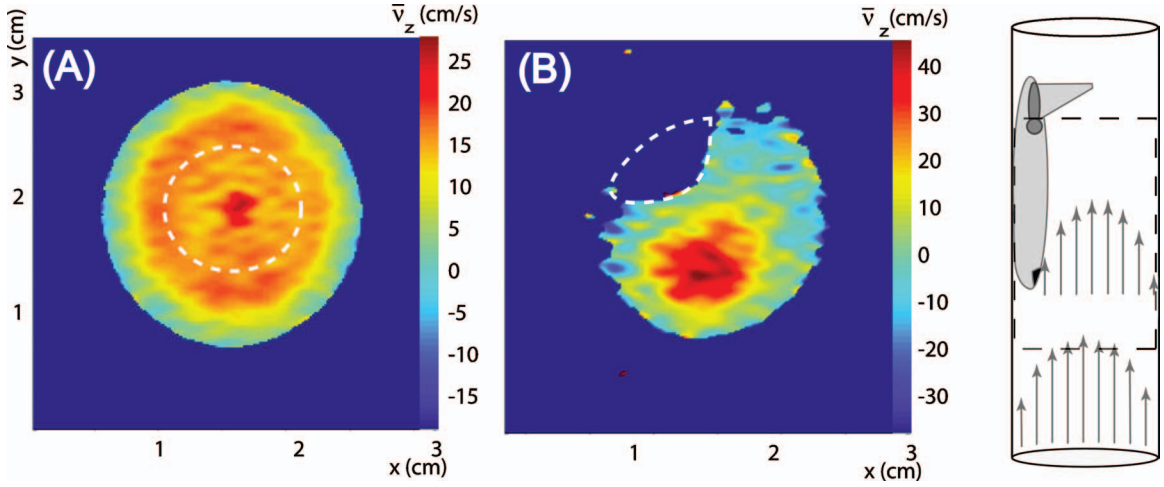

FIG. 2. (Color) ^{129}Xe MRI velocity maps of flow around blunt and aerodynamic bodies displayed across the xy cross section. (a) Velocity map of v_z as a function of x and y at Re=100 with a maximum velocity of around 18 cm/s. The flattened profile depicted in the v_z versus xy map projected over the z axis around the ball volume, arises from the transverse velocity components as the gas maneuvers around the sphere [see sketch in Fig. 1(d)]. As expected for disruptive nonlaminar flow, the longitudinal flow velocities are equalized over a large cross section of the tube. (b) Velocity map of v_z as a function of x and y of gas flow around a model airplane body attached with its length axis along the wall at one side of the tube, as shown in the sketch on the right. The v_z velocity distribution over the xy cross section retains a parabolic laminar pattern as expected in these Re regimes, albeit shifted off center due to the presence of the aerodynamic toy body.

ment to be around 200. The airplane body carried out at a Re measured to be around 250.

The Re of the gas was calculated according to $\mathrm{Re}=(\bar{v}\cdot\bar{d}\cdot\bar{\rho})/\bar{\eta}$, where $\bar{v}$, $\bar{d}$, $\bar{\rho}$, and $\bar{\eta}$ are the average velocity, length scale of the system, density, and dynamic viscosity of the flowing medium respectively. $\bar{\rho}$ and $\bar{\eta}$ were calculated from the average mass, $\bar{M}$, and diameter of the particles, $\bar{\phi}$, according to $\bar{\rho}=(\bar{M}\cdot P\cdot 1000)/k\cdot T$ and $\bar{\eta}=(5\pi/16)\cdot\sqrt{k\cdot T/\pi\cdot\bar{M}}\cdot(\bar{M}/\pi\cdot\bar{\phi}^2)$, where k is the Boltzmann constant, P is the total pressure, and T is the absolute temperature of the system. This is equivalent to calculating the relevant weighted average of $\mathrm{Re}_{\mathrm{Xe}}$, $\mathrm{Re}_{\mathrm{N2}}$, and $\mathrm{Re}_{\mathrm{He}}$. [31].

DISCUSSION

Velocity encoded images (3D) and velocity vector maps (4D) visualizing ^{129}Xe gas flow dynamics by MRI velocimetry are presented for two model systems: a solid sphere suspended in a tube, Figs. 1(a)–1(c) and 2(a), and an aerodynamic airplane body, Fig. 2(b). The velocity encoded images are displayed as 2D spatial images, xz cross section in Fig. 1 and xy cross section in Fig. 2, with color-coding corresponding to longitudinal velocity values in cm/s at each pixel of the image. Figures 1(a), 1(b), and 2(a) correspond to the measurement made at Re=100 while Fig. 1(c) represents a higher Re of around 200. The velocity vector map is a 4D map [Fig. 1(b)] reconstructed from the v_z [Fig. 1(a)] and v_x (not shown here) velocity encoded 2D images. The black arrows represent velocity vectors composed of v_z and v_x components which are overlaid with the spin density image displaying the position of the sphere [Fig. 1(b)].

In the region below the sphere at Re=100, as expected for undisturbed pipe flow, the maximum velocity is in the center of the tube with near-zero velocities at the walls. As the gas reaches the sphere, its path diverges and we see regions of fast flow more laterally along the walls of the tube [Fig. 1(a)]. The flow rate predicts a maximum velocity of approximately 18 cm/s as is confirmed in the experimentally measured velocity values shown in the color map (red shading on both sides of the sphere). Immediately behind the ball, there is a region of lower longitudinal, v_z, velocity shown in green, indicating the presence of greater transverse velocity. Even though the observation of low longitudinal flow is somewhat indirect, the smooth nature of the pattern at this Re excludes effects of incoherent longitudinal fluctuations or stable turbulent flow, and strongly supports coherent, nonlaminar patterns, most likely recirculation eddies. Because of spherical symmetry, we are not be able to discriminate the details using projections, however, the retention of longitudinal velocity in the form of two trails separated by a low v_z region fits the expected recirculation flow pattern.

Direct measurements of transverse flow support the observations at Re=100 with the strongest contribution immediately before and behind the ball. The v_x encoded xz image is not shown, but it is combined with the v_z encoded xz image [Fig. 1(a)] to create the velocity vector plot shown in Fig. 1(b). Arrows represent the average behavior of a few pixels, and following them shows the streamlines are undisturbed in the lower part of the tube, diverge when encountering the ball, and begin to converge inwards from the sides after the ball. On the leading edge, the transition is quick and the region of transverse flow is short as the gas maneuvers around the sphere. On the trailing edge, however, the longitudinal components are not immediately recovered and transverse components persist and the flow field seems to converge after the sphere and then diverge again, oscillating to the edge of the field of view. This hysteresis in the upstream and downstream flow may indicate the beginning of more

complex dynamics in the far wake. As illustrated in Fig. 1(d), at $\mathrm{Re} > 1$, we would expect to see recirculation flow after the sphere. Employing slice selection to make finer measurements may reveal these characteristics, however, the broad feature, retention of transverse components after the sphere, is evident.

In an attempt to reach higher Re and other flow regimes, the flow rate was increased to the maximum value of the rotameter, but the reading was beyond its scale so that the flow rate could only be estimated before the experiments. As expected, considerably higher velocities were measured in Fig. 1(c). On first glance, the region around the sphere is similar to the lower Re measurement: fast streamlines on either side of the sphere and a lower longitudinal velocity right behind the sphere. However, the trails do not seem to persist as long as they did at the lower flow rate, and perhaps this is the beginning of more complex dynamics in the far wake. Additionally, the pattern on the leading edge is much different and takes a more flattened profile instead of the parabolic laminar pattern. Although the flow rate was not accurately known, from the NMR measured velocities, a Re of approximately 200 was determined.

The v_z encoded cross-sectional xy images in Fig. 2 illustrate the difference in disruption to the flow profile that blunt bodies make compared to aerodynamic ones. The creation of transverse components as the gas maneuvers around the ball results in a longitudinal velocity distribution that is nearly equalized across the diameter of the tube. This appears as a flattened v_z profile, illustrated by the red color which dominates the image [Fig. 2(a)]. In contrast, gas flow over an aerodynamic model airplane body attached to the tube wall, seen as a cutout in the image, retains the characteristic parabolic v_z distribution for laminar flow albeit shifted off-center [Fig. 2(b)]. Despite the higher measured velocity, corresponding to Re around 250, the aerodynamic body has a less disruptive effect on the overall flow pattern.

Only coherent and time-invariant flow phenomenon, on the time scale of the total experimental time, could be displayed with such two-dimensional velocity vector maps. The necessity of coherent flow is imposed because the two-dimensional spatial and velocity information has to be mapped in a multi-dimensional fashion over the entire 17 min experimental period. In this experiment, the duration of the velocity encoding gradients, which determines the accuracy of velocity encoding, was only 150 μs and the duration between two velocity encoding pulses, which determines the velocity range and resolution, was $\sim$2 ms. The effect of incoherent flow would be canceled out over the course of the experiment. This means, on the one hand, that coherent and time-invariant flow patterns persist throughout the entire flow imaging sequence and, on the other hand, that we cannot exclude underlying complex, time-variant patterns, and finer slices of the flow field may yield additional information.

CONCLUSION AND OUTLOOK

We suggest a methodology for experimental visualization of coherent mass flow of gas that is powerful and versatile. Flow through, over, and around arbitrary channel geometries, objects, and obstacles can be displayed in a quantitative fashion. The noninvasive and multidimensional MRI velocimetry modality, coupled with hyperpolarized ^{129}Xe gas, offers promising insight into fluid mechanics problems by allowing direct visualization of flow in complex geometries of length scale ranging from 1 μm up to $\sim$10 cm. Finer features in the flow field can be accessed by sampling thinner slices. Additionally, by exploiting the high chemical sensitivity of ^{129}Xe upon inclusion into, or interaction with, a wide range of materials and physiochemical environments, a spectroscopic dimension may be added to the velocity map, providing insight into multiphase flow and catalytic applications.

ACKNOWLEDGMENTS

This work was supported by the Director, Office of Science, Office of Basic Energy Sciences, Materials Sciences of the U.S. Department of Energy under Contract No. DE-AC03-76SF00098. S. Han gratefully acknowledges the Humboldt Foundation for postdoctoral support.

[1] S. Stapf and S. Han, eds., *Nuclear Magnetic Resonance Imaging in Chemical Engineering* (Wiley-VCH, Weinheim, 2005).
[2] L. F. Gladden, AIChE J. **49**(1), 2 (2003).
[3] Y. Takeda, Exp. Therm. Fluid Sci. **10**, 444 (1995).
[4] S. Manneville, L. Becu, and A. Colin, Eur. Phys. J.: Appl. Phys. **28**, 361 (2004).
[5] E. Guyon *et al.*, *Physical Hydrodynamics* (Oxford University Press, New York, 2001).
[6] E. Fukushima, Annu. Rev. Fluid Mech. **31**, 95 (1999).
[7] R. Kimmich, *NMR Tomography, Diffusometry, Relaxometry* (Springer, Berlin, 1997).
[8] Song-I Han, S. Stapf, and B. Blümich, Phys. Rev. Lett. **87**(14), 144501 (2001).
[9] B. Newling, C. C. Poirer, Y. Zhi, J. A. Rioux, A. J. Constire, D. Roach, and B. J. Balcom, Phys. Rev. Lett. **93**(15), 154503 (2004).
[10] A. J. Sederman *et al.*, J. Magn. Reson. **166**, 182 (2004).
[11] L. G. Kaiser *et al.*, Proc. Natl. Acad. Sci. U.S.A. **97**(6), 2414 (2000).
[12] I. L. Moudrakovski *et al.*, J. Magn. Reson. **144**, 372 (2000).
[13] L. G. Kaiser *et al.*, J. Magn. Reson. **149**, 144 (2001).
[14] K. Ruppert *et al.*, Magn. Reson. Med. **44**, 349 (2000).
[15] B. Saam *et al.*, Magn. Reson. Med. **42**, 507 (1999).
[16] M. J. Lizak, M. S. Conradi, and C. G. Fry, J. Magn. Reson. (1969-1992) **95**, 548 (1991).
[17] R. Wang, R. W. Mair, M. S. Rosen, D. G. Cory, and R. L. Walsworth, Phys. Rev. E **70**, 026312 (2004).
[18] R. W. Mair, C. H. Tseng, G. P. Wong, D. G. Cory, and R. L. Walsworth, Phys. Rev. E **61**, 2741 (2000).
[19] D. O. Kuethe *et al.*, J. Appl. Physiol. **88**, 2279 (2000).

[20] I. V. Koptyug *et al.*, J. Magn. Reson. **147**, 36 (2000).
[21] S. D. Beyea *et al.*, Magn. Reson. Imaging **21**, 201 (2003).
[22] J. Granwehr, E. Harel, S. Han, S. Garcia, A. Pines, P. N. Sen, and Y. Q. Song, Phys. Rev. Lett. **95**, 075503 (2005).
[23] Q. Lin *et al.*, J. Fluid Mech. **240**, 315 (1992).
[24] H. Sakamoto and H. Haniu, J. Fluids Eng. **112**, 387 (1990).
[25] D. Ormières and M. Provansal, Phys. Rev. Lett. **83**(1), 80 (1999).
[26] T. A. Johnson and V. C. Patel, J. Fluid Mech. **378**, 19 (1999).
[27] E. Achenbach, J. Fluid Mech. **62**, 209 (1974).
[28] S. Taneda, J. Phys. Soc. Jpn. **11**, 1104 (1956).
[29] W. Happer, E. Miron, S. Schaefer, D. Schreiber, W. A. van Wijngaarden, and X. Zeng, Phys. Rev. A **29**, 3092 (1984).
[30] M. Haake *et al.*, J. Am. Chem. Soc. **119**, 11711 (1997).
[31] I. F. Golubev, *Viscosity of Gases and Gas Mixtures* (transl. Israel Program for Scientific Translation, Jerusalem, 1970).